Detached Eddy-Simulations of Delta-Wing Post-Stall Flow Control

Buzica Andrei
Technical University of Munich, Department of Mechanical Engineering
Research Engineer
Boltzmannstr. 15, 85748-Garching b. München, Germany
andrei.buzica@yahoo.com

Biswanger Manuel
Technical University of Munich, Department of Mechanical Engineering
Graduate Student

Breitsamter Christian
Technical University of Munich, Department of Mechanical Engineering
Chief Scientist

ABSTRACT

Flow control can significantly improve the aerodynamic performances of delta wings. Yet, despite numerous studies of vortex control by leading-edge blowing still little research is focused on the post-stall regime and further consideration of the shear-layer reattachment through flow control is needed. This paper reports on the effects of unsteady jets on the global flow field at a very high angle of attack, $\alpha = 45°$. For this, Detached-Eddy Simulations are conducted and validated with wind tunnel test results. The vortex shedding of the unperturbed delta-wing flow is investigated and compared to the perturbed case. It concludes that unsteady blowing energizes the shear layer and reorders at the same time the shedding mechanism eventually forming a big burst vortex structure that increases the lift significantly.

KEYWORDS: *Delta Wings, Flow Control, Post-Stall, DES*

NOMENCLATURE

Latin
C_L - Lift coefficient
DC - Duty cycle
F^+ - Dimensionless frequency
Q - Q-criterion
Re - Reynolds number
$S^N_{u/U}$ - Power spectral density of the dimensionless axial velocity
U - Velocity magnitude
c_r - Wing root chord
d - Grid spacing
f - Frequency
h_{min} - Minimum cell height
l_μ - Mean aerodynamic chord
k - Reduced frequency
s - Wing's half span
ts - Time step number
u - Axial velocity
x, y, z - Wing's cartesian coordinates
y^+ - Wall normal distance in wall units

Greek
Λ - Wing's aspect ratio
Δx - Mean longitudinal surface grid spacing
Δt - Time step size
α - Angle of attack
δ - Wing's thickness
φ - Leading-edge sweep angle
ω_x - Axial vorticity

Subscripts
avg - Time-averaged
l - Local
rms - Root mean square
∞ - Freestream condition

1 INTRODUCTION

Large counter-rotating vortices dominate the flow around delta wings. These vortices are generated by the shear layer leading-edge separation and subsequent rollup. These large scale vortices produce non-linear additional lift compared to wing configurations with mainly attached flow. Thus, delta wings demonstrate superior maneuverability. In addition, these wing configurations reach generally higher maximal angles of attack.

The high angle of attack flow field is, however, very unsteady, which limits the flight envelope. An extension of this may be achieved through flow control. There are several vortex-flow control methods, which are categorized in passive–active and steady–unsteady systems [1]. While many investigations focus on the delay of the vortex breakdown [2], very few studies investigate the flow control in the post-stall regime, where a large separation region dominates the flow field [3]. Prior to the current work, Research investigating this phenomenon experimentally demonstrated the shear layer reattachment on the wing's upper surface at $\alpha = 45°$, when pulsed blowing at the leading edge was active. The investigated flow control mechanism comprises of stepwise fluid injection through pairwise slots located near the leading edge. The jets are injected almost normal to the wing with a reduced actuation frequency of $F^+ = f \cdot c_r/U_\infty = 1.0$. With this actuation strategy, a lift increase of more than 50% is possible [4]. The phase-averaged velocity field of the actuated case demonstrated the existence of vortices that stabilize the flow.
The current work complements the mentioned investigation numerically, with Detached-Eddy Simulations (DES). The scale resolving capability predicts more accurately the turbulent structures present in the transient flow field than the viscosity turbulence models. Therefore, the structure of the transient flow field and the underlying mechanisms, as the jet–flow interaction and the shear layer reattachment, are closely investigated. Furthermore, the numerical method is validated by wind tunnel tests (WTT).

2 NUMERICAL SETUP

The investigated delta wing represents the geometry defined in the Second Vortex-Flow Experiment project (VFE-2) [5]. The leading-edge is sharp and has a sweep angle of $\varphi = 65°$. The wing measures 0.977m at its root chord c_r, has an aspect ratio of $\Lambda = 1.87$ and has a relative wing thickness of $\delta/c_r = 3.4\%$. Near the leading-edge, on the upper side, high aspect ratio ($2\text{mm} \times 10\text{mm}$) blowing slots are located and arranged pairwise in three segments as shown in Fig. 1 (left). Through these nozzles, pulsed jets are injected into the outer flow in order to achieve a beneficial flow control.
The perturbed and unperturbed flow field around the delta wing is computed in the domain shown in Fig. 1 (right). The model of the investigated delta wing is situated at $5c_r$ away from the inlet surfaces (red colour), in front and beneath, and from the opening at the side (blue), where undisturbed flow is assumed. At the inlet, the freestream velocity of $U_\infty = 12\ \text{m/s}$, corresponding to a Reynolds number based on the mean aerodynamic chord ($l_\mu = 0.651$) of $\text{Re} = 0.5 \cdot 10^6$, and the angle of attack of $\alpha = 45°$ are defined. The outlet boundary condition (violet) is set at $10c_r$ downstream from the apex of the wing, both in horizontal and longitudinal direction. Symmetry of the flow problem is assumed, as asymmetric vortex interaction for this type of delta-wings, with moderate leading-edge sweep angles, is negligible [6]. This reduces valuable computational resources. The péniche is not modeled here, thus the symmetry boundary condition is located at $y/s = 0$.
Two cases are investigated in this work: the baseline and the actuated case. For the baseline case, the inlet surfaces of the slots are defined as walls. As for the actuated case, these surfaces are modelled as inlets. The effect of pulsating jets on the flow field is, thus, investigated. The modeled flow control mechanism induces simultaneously jets into the outer flow with a frequency of $f = 12$ Hz, corresponding to a reduced frequency of $F^+ = 1.0$. The duty cycle of the actuation is set at $DC = 25\%$, defining the relative amount of time during one blowing period in which the jets are active. During the active quarter period, the jets have a velocity of $60\ \text{m/s}$

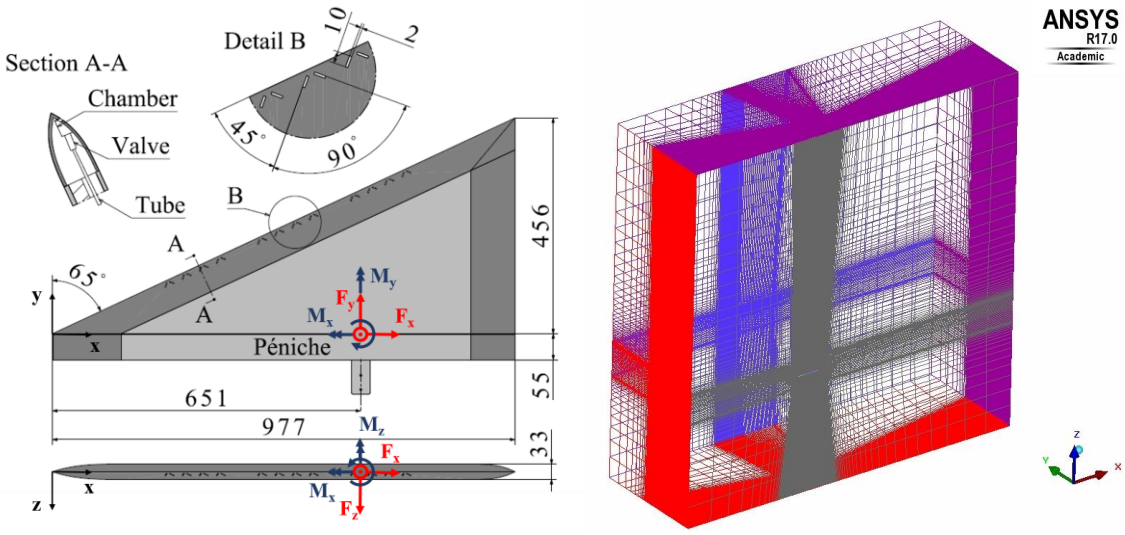

Figure 1: Wing model (left) [4] and computational domain (right).

and are oriented almost perpendicular to the wing's planform. This actuation mode has shown great potential in reattaching the separated flow on the wing's upper surface and, thus, increasing the lift coefficient significantly [4].

The computations include solving the Navier-Stokes equations with the commercial pressured-based solver ANSYS FLUENT. The solver accelerates the solution convergence with the implemented Algebraic Multigrid algorithm and the segregated pressure–velocity coupling algorithm SIMPLE. This solves iteratively the continuity equation updating the pressure field accordingly [7]. First, steady Reynolds-Averaged Navier–Stokes (RANS) solutions are obtained. The turbulence is closured by the two-equation $k-\epsilon$ −realizable model [7]. The spatial discretization is second order accurate and the gradients at each cell face are evaluated with the Green–Gauss Cell Based method. Second, DES computations are conducted initialized by the converged steady solutions. The convergence criterion of all residuals is 10^{-4}. The advancement in time is achieved with the dual-time stepping algorithm. Therefore, the Bounded Second-Order Implicit Time Integration is employed. Three time step sizes are evaluated in the current study: $\Delta t = 1.1 \cdot 10^{-4}$ s, $2.1 \cdot 10^{-4}$ s and $4.2 \cdot 10^{-4}$ s. This corresponds to different divisions (800, 400, and 100, respectively) of one blowing period ($T = 1/f = 0.08\overline{3}$ s). The CFL number ($\Delta t \cdot U_\infty/\Delta x$) above the wing is consequently in the range 0.5–2.0. All computations are parallelized and executed on 140 cores of the Leibniz Supercomputing Centre (SuperMUC).

DES is a hybrid computational method that switches between RANS and Large Eddy Simulation (LES) based on the grid spacing. This method is well established for flow problems with large separation regions, i.e. stalled wings. The boundary layer is modelled in the computationally efficient RANS mode, while the turbulent structures in the unstable flow regions are resolved with LES. The version of the employed turbulence model is the Detached DES with the Shear Stress Transport model for RANS (DDES-SST) [8]. This improves the accuracy by avoiding unphysical grid induced separations.

The domain is discretized with the meshing software ANSYS ICEM in a block-structured manner. Three O-grids are placed around the wing, defining the boundary layer (≈ 3 mm), the LES region (≈ 27 mm) and the transition zone (≈ 190 mm) [9]. The wall nearest spacing is set at around $h_{min} = 0.01$ mm, thus, a distance in wall units of $y^+ < 1$ is achieved. The exponential cell growth ratio away from the wall is set at approximately 1.2. For the grid independence study three grids with different refinements are assessed. The main difference between the grids is the cell count in the second and third O-grid. Important grid parameters are summarized in Table 1.

Fig. 2 shows the blocking around one blowing slot pair and the coarse mesh around the delta wing. This meshing strategy allows a local grid refinement around the wing, which is necessary for an accurate solution in the LES region. The finest grid is refined, additionally above the blowing slots.

Table 1: Characteristics of the computational grids.

Grid		**Coarse**	**Medium**	**Fine**
Total	Nodes	$23 \cdot 10^6$	$49 \cdot 10^6$	$66 \cdot 10^6$
	Computed time/iteration	1.4 s	3.1 s	4.0 s
1nd O-grid	Wall normal node count	29	29	29
	Minimum cell spacing	0.01 mm	0.01 mm	0.01 mm
	Exponential growth ratio	1.13	1.13	1.13
2nd O-grid	Wall normal node count	16	32	40
	Minimum cell spacing	0.48 mm	0.48 mm	0.48 mm
	Exponential growth ratio	1.30	1.04	1.03
3rd O-grid	Wall normal node count	15	60	80
	Minimum cell spacing	3.57 mm	1.30 mm	0.88 mm
	Exponential growth ratio	1.30	1.04	1.03

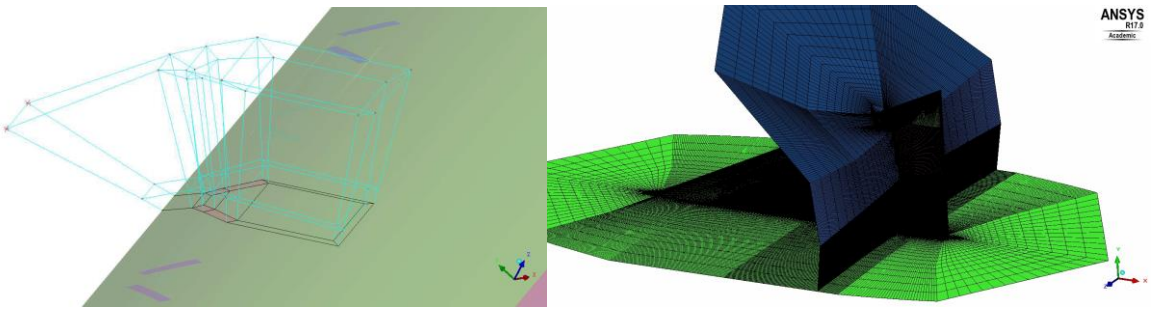

Figure 2: Blocking above one slot pair (left) and coarse O-grid around the delta wing (right).

3 RESULTS AND DISCUSSION

3.1 Grid Independence Study

The steady state solution of the baseline case computed on different grids is shown in Fig. 3. The flow field constitutes of a large separation region. The shear layer that forms from the separation of the pressure-side boundary layer is characterized by high vorticity values. Here, the vorticity is nondimensionalized by the ratio of the freestream velocity U_∞ and the mean aerodynamic chord l_μ. The shear layer is naturally unstable and promotes the formation of discrete vortices (Kelvin-Helmholtz instability). Hence, a steady state solution is never reached. However, by comparing all three quasi-steady solutions the capability of capturing relevant physical processes can be assessed. According to the contour plots of Fig. 3 the shear layer instability is captured only in the medium and the fine mesh. The coarse grid is obviously too dissipative in order to resolve the turbulent structures. In addition, unphysical, grid-caused discontinuities are observed in the left plot.

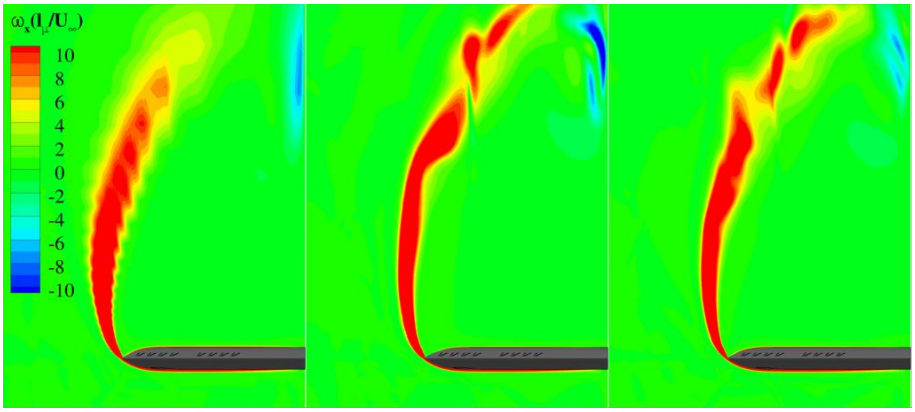

Figure 3: Results of RANS computations of the baseline case showing the out-of-plane dimensionless vorticity in the crossflow plane at $x/c_r = 0.6$ on the coarse, medium and fine grid (from left to right) after 125300 iterations; $Re = 0.5 \cdot 10^6$, $\alpha = 45°$.

Fig. 4 displays the convergence of the lift coefficient resulting from the steady simulations on the investigated grids. The measured lift coefficient of the baseline case ($C_L = 0.58$) [4] is under-predicted. This is expected from the steady method, which cannot resolve the turbulent structures and recreate the correct pressure distribution on the wing's upper surface. Despite of this, the convergence history concludes that a mesh refinement leads to a C_L convergence towards a higher value. In addition, taking aside the difference in computational cost (see Table 1), all three graphs have similar convergence slopes. As a consequence, the unsteady simulations are conducted on the medium grid initialized with the respective steady solution. It represents correctly the flow physics (see Fig. 3), unlike the coarse grid, and requires less computation effort than the fine grid. As discussed in Section 3.5, during the transient computations the lift increases above the measured values.

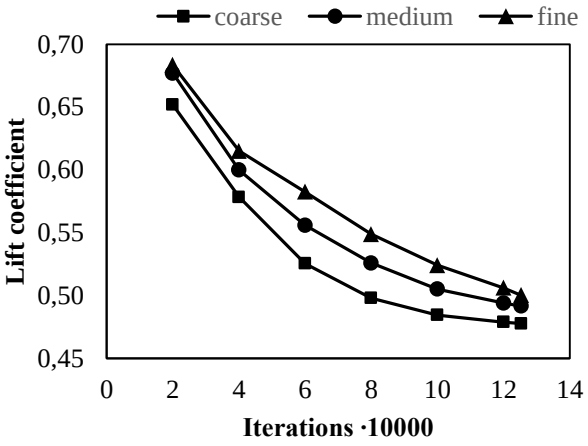

Figure 4: Convergence of the lift coefficient from RANS computations on differently refined grids—Baseline case.

3.2 Time Step Study

The time step study is conducted with the medium refined computational mesh and initiated with the steady solution obtained after 125300 iterations. As seen in Fig. 3, the flow field is already developed and represents a suitable initial condition for the transient simulation. The lift coefficient is again monitored throughout the computations in Fig. 5 for the baseline case. Here, it is plotted as function of time step number. The quasi-random fluctuating lift coefficient curve demonstrates high flow unsteadiness. Increased time advancement is observed when using the largest time step size. This also comes with a cost: around 15 iterations per time step are required until convergence of the transport-equation residuals. In contrast, a two times lower Δt requires 8

inner iterations. The transient results shown below are obtained with the lowest Δt ($1.1 \cdot 10^{-4}$ s). After the simulation start-up, convergence is reached for this setup after two inner iterations per time step. This is computationally more efficient and has the best temporal accuracy in order to resolve the unsteady flow structures.
The same temporal and spatial discretization has been employed as well for the actuated case, in which unsteady fluid injection is implemented as inlet boundary conditions. The transient computations are also initialized from a steady solution, in which steady blowing through all slots is computed. This accelerates significantly the formation of a statistically converged flow field. At almost all time steps the transport equation residuals converge after 9 iterations (7 more than the baseline).

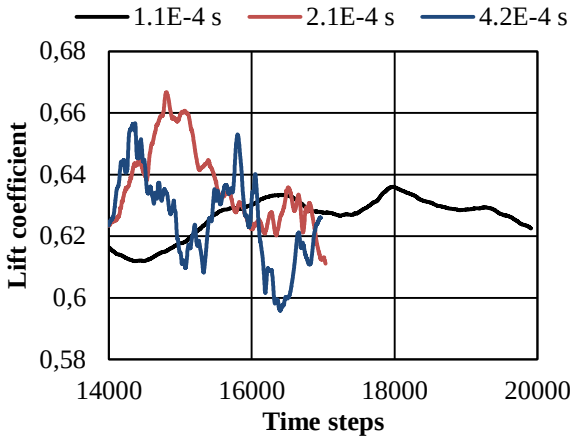

Figure 5: Lift coefficient versus iterations for three different time step sizes—Baseline case.

3.3 Time-Averaged Flow Field

The results shown in this section are obtained from DES computations of the baseline and actuated ($F^+ = 1.0$) case. After reaching a quasi-steady state, the flow statistics are calculated from a period of 0.9 s simulated time (corresponding to 11 blowing periods). For both cases the nondimensional time step size and streamwise grid spacing measure $\Delta t \cdot U_\infty / c_r = 1.3 \cdot 10^{-3}$ and $\Delta x / c_r = 2.4 \cdot 10^{-3}$, respectively. According to [9] this should resolve well the relevant turbulent structures. For validation purposes the CFD results are compared to wind tunnel measurements. The measurements were conducted by recording 400 samples with a frequency of 13 Hz, resulting in an averaging time of around 30 s [4]. Therefore, very low frequency fluctuations of the complete flow field are recorded in addition to the numerical simulations. These are not discussed here, as the focus in this paper lies on the unsteady flow phenomena with a reduced frequency in the order of $F^+ = O(1)$.
Fig. 7 presents the time-averaged flow field at the very high angle of attack of $\alpha = 45°$ and $Re = 0.5 \cdot 10^6$. The mean values of the dimensionless vorticity distribution in the crossflow plane at $x/c_r = 0.6$ are shown in the range $-10 \leq \omega_{x,avg}(l_\mu / U_\infty) \leq 10$. The undisturbed flow field (Baseline) represents the above mentioned shear layer formation separated from the leading edge. This itself is naturally unstable and sheds discrete vortices, as discussed in Section 3.4. Above the wing, a typical dead water region is present, generating a low constant pressure coefficient distribution (see Fig. 6). The computational method predicts well the shear layer creation with high concentrated axial vorticity values at the leading edge, which decrease downstream, indicating flow unsteadiness. The particle image velocimetry (PIV) plane (left lower image) captures the averaged flow field with an increased thickness compared to the CFD results. The reason can be in the increased averaging period.
When pulsed blowing is active (Actuated) the induced disturbances interact with the shear layer provoking a stronger inwards deflection and a premature decay in discrete vortices. These are transported in a clockwise-spiraling trajectory towards the wing's upper surface. On a big scale, a burst vortex is formed. This is characterized by the nearly annular axial vorticity distribution $\omega_{x,avg}(l_\mu / U_\infty) \geq 6$ in cross section. The flow structure induces near-wall velocities that increase suction on the wing's upper side (see Fig. 6). Consequently, the boundary layer on the upper surface is formed, distinguished by the negative axial vorticity regions. This increases in thickness towards the leading edge promoting wall separation.
The pressure coefficient is plotted in Fig. 6 against the local relative wing span at 0.4, 06 and 0.8 relative root chord sections. Wind tunnel results are extracted from [10]. A constant mean suction level and low fluctuations are present above the wing. This is generated by the dead-water region enclosed by the shear layer. Its reattachment produced by the pulsating leading-edge jets causes an increase in suction with flat peaks at around 60% local span, excluding the apex region. In addition the r.m.s. pressure coefficient increases by almost one order of magnitude. Its spanwise distribution has peaks further inward, at around 30% local span. Both mean and r.m.s. pressure coefficient decrease chord wise, related to the vortex expansion.
Towards the leading edge local r.m.s. peaks are present. Here, the local flow is unsteady due to the disturbance injection and due to the wall separations. The computed pressure distribution is in good agreement with the experiment. Slight deviations are recorded near the apex.

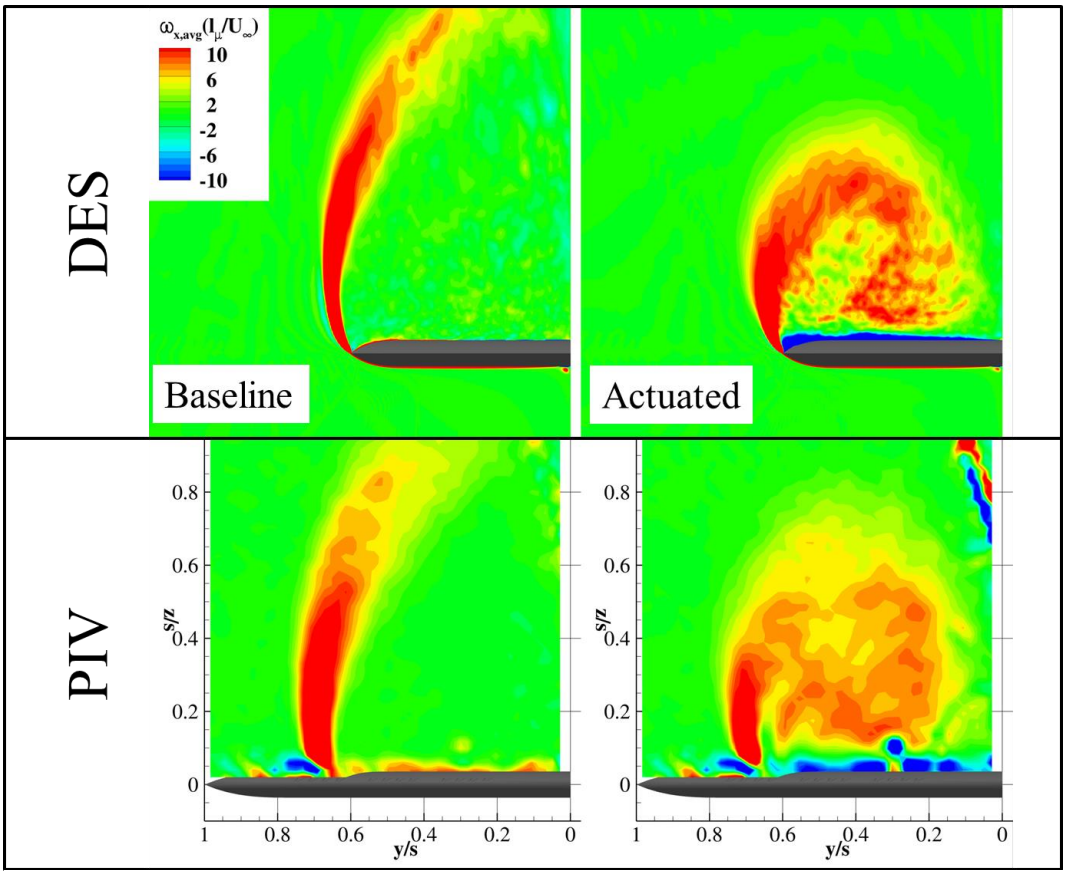

Figure 7: Out-of-plane dimensionless vorticity distribution at $x/c_r = 0.6$. Baseline and Actuated case with a reduced frequency of $F^+ = 1.0$. Comparing DES with PIV results. $\alpha = 45°$, $Re = 0.5 \cdot 10^6$.

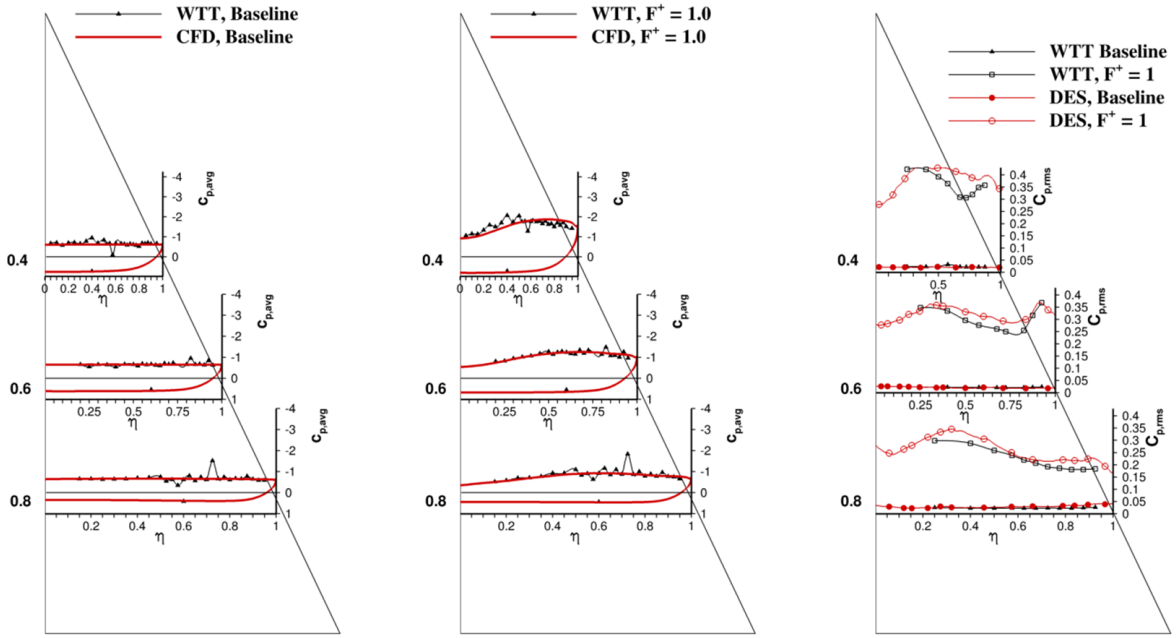

Figure 6: Spanwise distribution of the pressure coefficient, average (left and mid) and r.m.s. (right), for the baseline and actuated ($F^+ = 1.0$) cases. Comparing DES and wind tunnel test (WTT) results. $\alpha = 45°$, $45°$, $Re = 0.5 \cdot 10^6$.

3.4 Transient Flow Field

After discussing the averaged flow field, the axial vorticity distribution at discrete time steps in the crossflow plane $x/c_r = 0.6$ is presented in Fig. 8. Both computed cases, baseline and actuated, are compared to an a priori sample (Frame 200) of the 400 recorded with PIV. The DES baseline case is shown at the last computed time step (ts). The actuated flow is shown at $ts = 605$ of the last computed blowing period (800 ts). Only during the first quarter of a period ($1 \leq ts \leq 200$) air is evacuated through the blowing slots. The PIV snapshot has been obtained from phase-locked PIV measurements, in which the sampling was triggered by the actuation step signal [4]. In the actuated case the measurement plane has a coarser sampling grid with a nondimensional spacing of $d/s_l = 3.3 \cdot 10^{-2}$, compared to the much finer resolution in the baseline case ($1.4 \cdot 10^{-2}$). Despite of this, peak vorticity regions are still depicted. These structures (referred to as vortices) are shed, as discussed above, from the separated shear layer and are transported downstream.

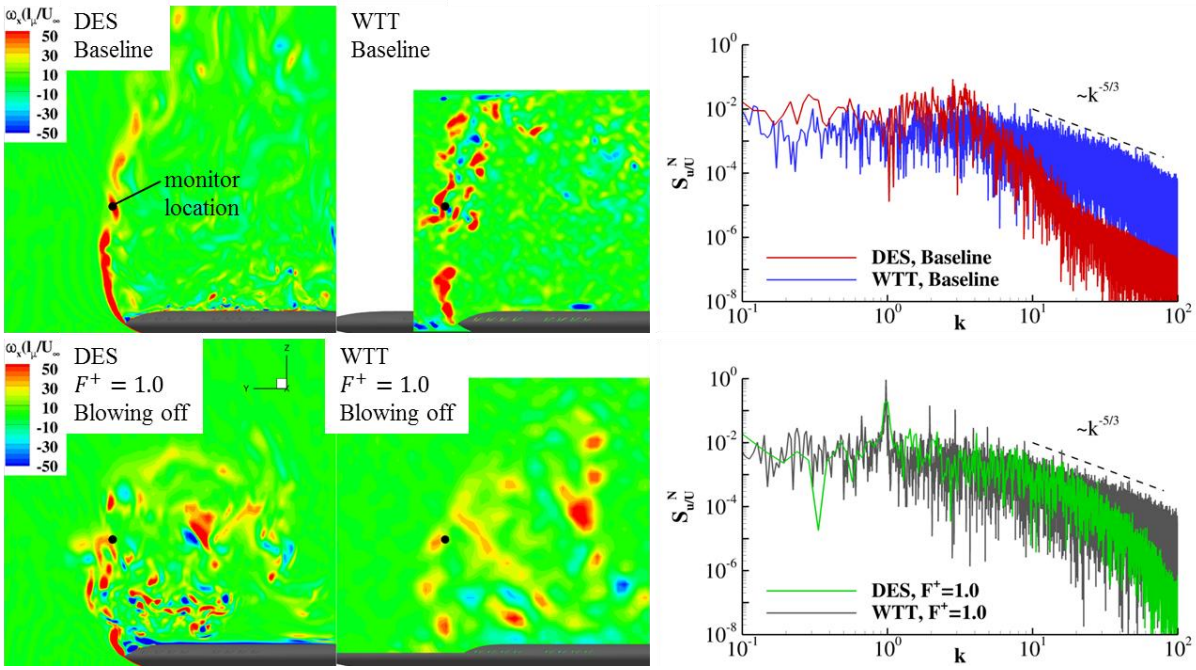

Figure 8: Right: instantaneous, out-of-plane dimensionless vorticity distribution in the crossflow plane $x/c_r = 0.6$ for Baseline and Actuated cases (DES and WTT). Left: PSD of the relative axial velocity against the reduced frequency *k* measured at the "monitor location" for the discussed cases.

The actuation deflects the shear layer with the shed vortices inboards and downwards. The vorticity peaks are distributed radially and nearly equally spaced. The structures present in the controlled case are bigger and farther apart from each other, compared to the uncontrolled case. The induced jets force the shear layer to prematurely shed vortices. These are overall larger in cross section and with higher vorticity values [11]. The CFD method reconstructs well the unforced and forced vortex shedding mechanism. Differences are observed in the shear layer thickness (Baseline) and the cross section diameter of the big scale structure (Actuated)—see also Fig. 7. The shear layer is thicker in the experiment and the shedding starts slightly earlier. Possible flow disturbance sources that increase the turbulence levels during the wind tunnel measurement (structural oscillation, low frequency background noise) can cause the differences. In addition, the WTT were conducted with the wind tunnel model connected to an underfloor balance and with a péniche in between that reduces the wind tunnel boundary layer influence on the delta-wing flow. With this péniche the flow is not as constrained as in the simulations.

Nevertheless, good agreements in the inspected flow fields are obtained. This is supported as well by the comparison of velocity spectra between CFD and hot wire measurements (measurement setup is presented in [12]). Fig. 8 (right) shows the power spectral density (PSD) $S^N_{u/U}$ of the relative axial velocity signal, monitored above the leading edge at the following relative wing coordinates: $x/c_r = 0.6, y/s_l = 1.057, z/s_l = 0.555$. This location is also marked in the aside crossflow planes. The PSD values are plotted against the reduced frequency $k = f \cdot c_r/U_\infty$ in double logarithmic representations.

The spectra of the baseline case show a nearly constant PSD level until $k \approx 3.5$, after which the values drop. This flat distribution demonstrates that the local flow field oscillates randomly, with no unique frequency. The shedding of the vortices is, hence, not ordered. Nearly distinguishable peaks may be found at $k \approx 4.2$, in the

experiments, and at $k \approx 3.4$, in the flow simulations. The hot wire apparatus records the typical turbulence scale decay with the exponent of $-5/3$ (also known as the Kolmogorov law). In the numerical investigations however, the slope differs from that distribution. The PSD values drop with a steeper slope in the range $3.5 \leq k \leq 20.0$ and the Kolmogorov decay is observed at higher frequencies. Hence, the spectral distribution of the energy contained in the turbulent scales is well predicted by DES at low frequencies and underpredicted at higher. This is traced back to the scale resolving capabilities of LES. This method resolves the scales larger than the grid spacing and models the subgrid scales. In other words, the grid "filters" the resolved flow field. A finer grid would resolve finer scales but with a considerably higher computational cost. For the current investigations the selected grid is fine enough in order to resolve the relevant, geometry-dependent flow structures.
With blowing, the spectral content changes. A clear peak associated with the blowing frequency is detected in both numerical and experimental investigations. The hotwire anemometry detects in addition to the DES two higher harmonic peaks ($k = 2.0, 3.0$). The PSD levels of the DES computation with blowing matches the measured ones. Above $k \approx 28$ the computed PSD slope starts to diverge from the experimental values. This is caused, as well, by the scale-resolving limit.
Fig. 9 shows the 3D flow fields at discrete time steps. The visualizations includes isosurfaces of the Q-criterion ($Q = 10^5\ s^{-2}$) coloured with the relative axial velocity u/U_∞. The baseline flow field at the last computed time step is represented in the first graphic. At the leading edge, coherent structures with positive axial velocities are shed. These are the product of the Kelvin-Helmholtz instability. The shedding starts at the apex and advances along the leading edge. Further downstream the shed, coherent vortices show 3D instabilities and vortex-vortex interactions. The flow inboard of the shear layer represents the dead-water region with low negative axial velocities and low turbulence.
The actuated flow (second and third representation in Fig. 9) is shown at two time steps (ts) of the last computed blowing period (800 ts), 105 and 605. Only during the first quarter of a period ($1 \leq ts \leq 200$), air evacuates through the blowing slots. As seen in the section above, the shear layer constituting of discrete vortices reattaches on the wing and forms on a big scale a burst vortex. On a smaller scale, the shedding mechanism is altered when the flow field is perturbed. The perturbations have a significant, upstream influence on the flow field, especially on the apex region. Here the quasi-steady shear layer is reattached and becomes unstable further downstream, eventually shedding vortices that twist counter clockwise around the low energy core, where $u/U_\infty < 0$. At $ts = 105$ of the last blowing period, the jets form discrete small eddies above the blowing segments (designated with arrows in Fig. 9). These eddies are transported into the shear layer, just after its formation, destabilizing the coherent structures and promoting their decay. This has several effects:

- increase of turbulent mixing between the outer, high-energy flow and the low-energy, core flow;
- kinetic energy increase in the shear layer, especially in circumferential direction leading to reattachment;
- ordering the vortex shedding, such that when a wave of disturbances exits the flow field above the wing the next disturbance is induced at the leading edge.

Even after fluid injection, during the inactive phase, the disturbances in form of small eddies persist above the blowing slots (see lower plot in Fig. 9). The rolled-up shear layer at the apex shows likewise a stable behaviour. This concludes that the burst vortex keeps its structure even after the perturbation injection.

3.5 Lift and Drag Coefficients

The resulting force coefficients are compared in Table 2. The DES computation overestimates these coefficients in both cases by over 7%. The major difference in the setup is the inclusion of the péniche in the experiment. The flow structure over the wing expands in this case over the symmetry plane, having its reattachment line on the péniche, where the aerodynamic loading is not measured. This expansion is noticeable in the larger flow structure measured in the crossflow PIV planes. The computed pressure distribution at the apex deviates as well slightly from the measured values. This proves that after separation in the apex region the shear layer is deflected beyond the symmetry plane, as there is no constriction, except the boundary layer displacement thickness. In future simulations this will be accounted for, in order to achieve a better agreement between CFD and WTT.

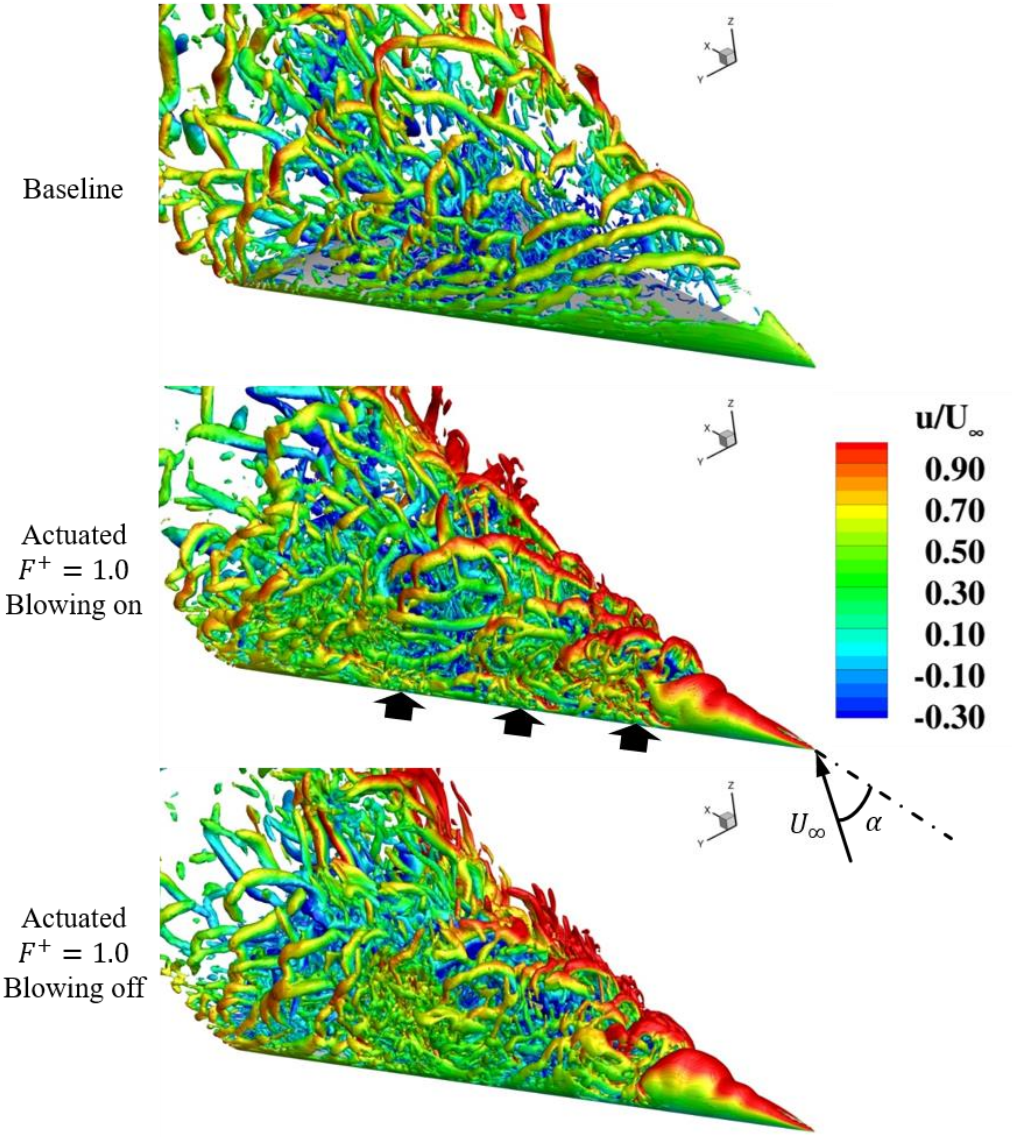

Figure 9: Q-criterion isosurfaces ($Q = 10^5$) coloured by the axial velocity u/U_∞ of the baseline and actuated cases (during and after fluid injection). $\alpha = 45°, Re = 0.5 \cdot 10^6$.

Table 2: Lift and drag coefficients.

		Baseline	Actuated	Delta
DES	Lift coefficient	0.63	1.00	0.37
	Drag coefficient	0.66	0.96	0.30
WTT	Lift coefficient	0.58	0.90	0.32
	Drag coefficient	0.62	0.85	0.23
DES-WTT [%]	Lift coefficient	8.1	10.3	15.6
	Drag coefficient	7.6	13.8	30.4

4 CONCLUSION AND OUTLOOK

The unperturbed and perturbed flow field around a 65° sweptback delta wing with freestream conditions of $\alpha = 45°$ and $\mathrm{Re} = 0.5 \cdot 10^6$ has been investigated numerically. Previous experiments showed that pulsed blowing at the leading edge in normal wing direction to the upper side reattached the otherwise separated shear layer. The performed DES computations complement this experimental data base, offering a better analysis of the underlying complex flow interactions.
The undisturbed flow field shows a stable shear layer at the apex, from which the separation of the vortices is initiated. The separation moves downstream. These coherent structures are as well unstable and decay into smaller vortices. With unsteady blowing at the leading edge the shear layer at the apex is reattached on the upper surface. The shedding frequency is reduced and the shed vortices increase in diameter and strength. The big scale burst vortex structure, a product of the actuation, constitutes of discrete vortices with different scales.
The shear layer interacts with jet vortices such that, on the one hand the circumferential momentum is increased and on the other hand, the vortex shedding mechanism is reordered. The jet vortices destabilize the shear layer and promote the premature vortex shedding. The vortices pair up while they are transported downstream in a clockwise spiraling path, caused by their interactions with each other and with the wing's upper surface. This mechanism describes the shear layer reattachment. The disturbances remain in the flow field even after injection and, on a big scale, the burst vortex structure shows a quasi-steady behavior.
The flow field and the induced pressure distribution are well predicted. The apex region shows slight deviations between experimental and numerical results. The integral values are, despite of this, higher than the measured ones. This is traced back to the use of a péniche during the wind tunnel tests. For future investigations a better agreement can be achieved by considering the boundary-layer displacement thickness of the wind tunnels floor in the CFD investigation.

ACKNOWLEDGEMENTS

The authors gratefully acknowledge ANSYS, Inc. for providing the simulation software, as well as the Gauss Centre for Supercomputing for computing time on the SuperMUC at Leibniz Supercomputing Center.

REFERENCES

[1] I. Gursul, Z. Wang, E Vardaki; 2007; "Review of Flow Control Mechanisms of Leading-Edge Vortices"; *Progress in Aerospace Sciences*; **43**(7); pp. 246–270
[2] A.M. Mitchell, J. Délery; 2001; "Research into Vortex Breakdown Control"; *Progress in Aerospace Sciences*; **37**(4); pp. 385 - 418
[3] N.J. Woods, L. Roberts; 1988; "Control of Vortical Lift on Delta Wings by Tangential Leading-Edge Blowing"; *Journal of Aircraft*; **25**(3); pp. 236–243
[4] A. Buzica, J. Bartasevicius, C. Breitsamter; 2017; "Experimental Investigation of High-Incidence Delta-Wing Flow Control"; *Experiments in Fluids*; **58**:131; pp. 1–16
[5] D. Hummel; 2008; "The Second International Vortex Flow Experiment (VFE-2): Results of the First Phase 2003–2008"; *26th Congress of the International Council of the Aeronautical Sciences*; ICAS 2008-3.3.1 (invited); Anchorage; September, 14–19
[6] E.C. Polhamus; 1971; "Predictions of Vortex-Lift Characteristics by a Leading-Edge Analogy";*Journal of Aircraft*; **8**(4); pp. 193–199
[7] ANSYS® Academic Research, Release 17.0, Help System, Fluent Theory Guide, ANSYS, Inc.
[8] F.R. Menter, M. Kunz; 2004; "Adaption of Eddy-Viscosity Turbulence Models to Unsteady Separated Flow behind Vehicles"; *The Aerodynamics of Heavy Vehicles: Trucks, Busses and Trains*; Springer, Berlin, Heidelberg; pp. 339–352
[9] P.R. Spalart, C. Streett; 2001; "Young-Person's Guide to Detached-Eddy Simulation Grids"
[10] A. Kölzsch, S. Blanchard, C. Breitsamter; 2016; "Dynamic Actuation for Delta Wing Post Stall Flow Control"; A. Dillmann, G. Heller, E. Krämer, C. Wagner, C. Breitsamter; *New Results in Numerical and Experimental Fluid Mechanics X. Notes on Numerical Fluid Mechanics and Multidisciplinary Design*; **132**; Springer, Cham; pp. 823–832
[11] J. Bartasevicius, A. Buzica, C. Breitsamter; 2016; "Discrete Vortices on Delta Wings with Unsteady Leading-Edge Blowing"; *8th AIAA Flow Control Conference*; AIAA Paper 2016-3170; Washington DC; June, 13–17
[12] A. Kölzsch, C. Breitsamter; 2014; "Vortex-Flow Manipulation on a Generic Delta-Wing Configuration"; *Journal of Aircraft*; **51**(5); pp. 1380–1390